High-spin spectrum of ^{24}Mg studied through multiparticle angular correlations

E. S. Diffenderfer,[*] L. T. Baby, D. Santiago-Gonzalez, N. Ahsan, A. Rojas,[†] A. Volya, and I. Wiedenhöver

Florida State University, Tallahassee, Florida 32306, USA

A. H. Wuosmaa

Western Michigan University, Kalamazoo, Michigan 49008, USA

M. P. Carpenter, R. V. F. Janssens, and C. J. Lister

Argonne National Laboratory, Argonne, Illinois 60439, USA

M. Devlin,[‡] D. G. Sarantites, and L. G. Sobotka

Washington University, St. Louis, Missouri 63130, USA

Y. Utsuno

Japan Atomic Energy Agency, Tokai, Ibaraki 319-1195, Japan

M. Horoi

Central Michigan University, Mount Pleasant, Michigan 48859, USA

We describe the investigation of high-spin states in ^{24}Mg populated with the ^{12}C(^{16}O, α)^{24}Mg reaction at 62- and 68-MeV beam energy. The excited states were established through the coincident detection of up to four α and γ particles in complete decay cascades toward a final state of angular momentum zero, the ground state of either ^{20}Ne or ^{16}O. We describe a new analysis method for the angular correlations in such events and apply it with the goal to assign spin and parity to α-unbound states in ^{24}Mg. We establish a number of high-spin, natural-parity states between spins 6 and 12, including the lowest known 10^+ and 12^+ levels. The energy systematics of positive- and negative-parity high-spin states are compared to the predictions of modern shell-model calculations.

PACS number(s): 27.30.+t, 21.10.Hw, 23.60.+e, 21.60.Cs

I. INTRODUCTION

The nuclide ^{24}Mg has been studied extensively since the early days of nuclear physics owing to its position on the chart of nuclides and its rich spectrum of excitations. This nucleus is sufficiently light to be calculated with microscopic models and sufficiently heavy to exhibit collective rotation. Therefore, ^{24}Mg serves as a rich testing ground for microscopic descriptions. The current interest in the shell structure of exotic nuclei has led to successful descriptions based on cross-shell configurations [1,2]. These extended shell-model calculations make it possible to study the competition between excitations of the main valence shell, in this case the sd shell, and the intruder excitations of the fp shell. In this context, the negative-parity spectrum and the states approaching spin 12, which is the maximum spin that can be generated within the positive-parity sd shell, promise to show most clearly the details of cross-shell configurations in the atomic nucleus. Another intriguing aspect discussed in the excitations of ^{24}Mg

is the presence of α and heavy-ion clustering, which has been the subject of a large number of publications. A recent review of this topic has been presented in Ref. [3].

A large number of experimental studies have been dedicated to the high-spin excitations of ^{24}Mg beyond the established 8^+ states. The states in question are particle-unbound by energies $\geqslant 5$ MeV and have complex decay paths, which make spin assignments challenging. Some experiments have, thus, concentrated on excitation function measurements and assigned quantum numbers based on calculations of the Hauser-Feshbach type (e.g., [4,5]). Because these calculations contain a number of adjustable parameters, extracted quantum numbers are usually accurate within, at most, one unit.

For ^{24}Mg states with their angular momentum aligned perpendicular with respect to the beam axis, the α-angular distribution populating the ^{20}Ne ground state exhibits an oscillatory pattern characteristic of the angular momentum L, given by a squared Legendre-polynomial of order L. The decay path of higher-lying states leads more often to excited final states, in which case the distribution of any single particle becomes uncharacteristic. The first examples of multiparticle angular correlation studies were described in Refs. [6–8], where the detection of a γ ray in coincidence with an α particle was shown to restore the characteristic high-L oscillatory patterns in the α angular distributions. All conclusive spin assignments to the α-decaying

---

[*]Present address: University of Pennsylvania, Philadelphia, Pennsylvania 19104, USA.

[†]Present address: TRIUMF, Vancouver, British Columbia, Canada V6T 2A3.

[‡]Present address: Los Alamos National Laboratory, Los Alamos, New Mexico 87545, USA.

high-spin states in ^{24}Mg originate in measurements of this type [6,8,9].

These early examples of α-γ angular correlation measurements observed γ rays with a single detector at a fixed angle. To establish more exotic and weakly populated excitations, methods to observe and analyze multiparticle coincidence events had to be developed. In the present work, we are describing two experiments which detected complete triple- and quadruple- particle decay cascades emitted from highly excited, high-spin states in ^{24}Mg. In these experiments, the angular momentum information is contained in the entanglement of the multiparticle final states, which is lost if any of the decay quanta remains undetected.

A straightforward analysis of the angular correlation information from these experiments would result in an impractically large number of angular bins and spectra with very low statistics. Angular correlation patterns would be very hard to observe or evaluate as a result. We, therefore, developed a more efficient analysis method based on an orthogonal basis transformation, which concentrates the same information into very few spectra. A similar analysis technique was described in Ref. [10], where it was applied to γ-γ angular correlations.

The paper is structured as follows. In Sec. II, we describe the experiments and the reconstruction of the ^{24}Mg excitations and their decay cascades. Section III develops the theory of multiparticle angular correlations and the principle of our data analysis, with some derivations described in Appendix Sec. II. The practical application of our basis-transformation analysis method is described in Sec. IV, along with examples of spin determinations. Section V summarizes the resulting spectrum of high-spin states from our measurements and compares the results with the literature. The implications of the newly established states for the mechanism of angular momentum generation within the sd shell and the onset of fp-intruder configurations is discussed in Sec. VI.

II. EXPERIMENTS

We studied the high-spin states of ^{24}Mg using the ^{12}C(^{16}O, α_0)^{24}Mg reaction in two separate experiments. Experiment A was performed at the ATLAS facility of Argonne National Laboratory using a beam energy of 62 MeV to study states decaying through α-γ and α-γ-γ cascades. The main results of the first application of the analysis technique, namely the identification of the 10_1^+ state and its γ-decay branch, were published as a conference proceedings article [11] and as a letter [12]. Here, we will summarize the results of experiment A and describe in more detail the analysis technique applied in it. Experiment B was performed at the superconducting linear accelerator laboratory of Florida State University, at a beam energy of 68 MeV to study higher-lying states, which decay through cascades with multiple α emissions.

A. Experiment A

We used an array of five double-sided silicon strip detectors (DSSDs) inside the Gammasphere detector array [13] to detect α particles emitted in coincidence with γ rays. The α particles
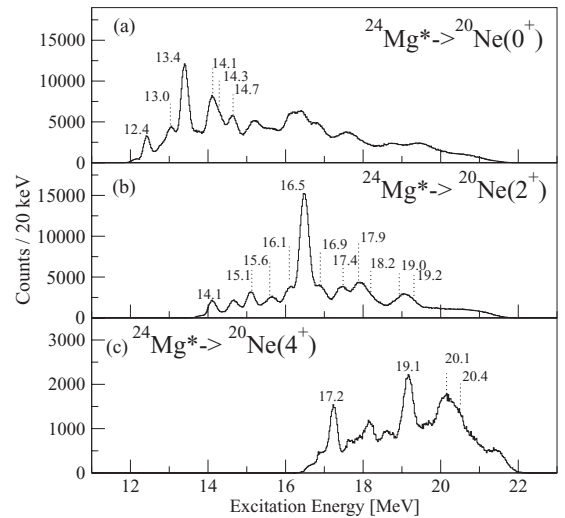

FIG. 1. Spectra of excited states observed in ^{24}Mg in experiment A, gated on their decay toward the 0^+ (a), 2^+ (b), or 4^+(c) states in ^{20}Ne. The excited states identified in the experiment are labeled with their excitation energy in MeV.

emitted from the ^{28}Si compound nucleus, denoted in this work as α_0, populate the states of interest in ^{24}Mg and establish their excitation energy. The α particles subsequently emitted from these states, denoted by α_1, and their angular distributions were detected in four 50×50-mm DSSDs with their centers positioned at angles $\theta = 45°$, $\phi = 45°$, $135°$, $225°$, $315°$ and at a distance of 117.5 mm from the target.

The excitation energy of ^{24}Mg was reconstructed using the spectrum of α_0 particles in an annular DSSD located 121 mm upstream from the target, covering angles in the range of $158°$–$168°$. The reaction kinematics suppress the emission of other particles toward backward angles, so that a very clean α spectrum is detected without additional particle identification. The two-body Q value of the α_0 and ^{24}Mg particles was reconstructed from the α_0 energy and angle. The coincident α_1 particles, emitted from states of ^{24}Mg, were detected in one of the four forward DSSDs. Their energy and angle was used to reconstruct the three-body Q value of α_0, α_1 and ^{20}Ne, herewith determining the final state populated in ^{20}Ne.

We observe population of bound states in ^{20}Ne, namely the lowest 0^+, 2^+, and 4^+ levels. Figure 1 displays the ^{24}Mg excitation energy spectra observed in experiment A, gated on the different ^{20}Ne final states. The spectra demonstrate that, with higher ^{24}Mg excitation energies and increasing angular momentum, the final state population shifts from the ^{20}Ne ground state to the 2^+ and 4^+ excited states.

The γ rays associated with the deexcitation of the 2^+ and 4^+ levels in ^{20}Ne were measured in coincidence using Gammasphere [13]. We recorded and analyzed the energy signals from the Compton-suppressor shields to achieve a higher detection efficiency than from the germanium crystals alone. Their resolution was sufficient to distinguish between the 2.614- and 1.633-MeV γ rays emitted from the 4^+ and 2^+ states of ^{20}Ne. The main information obtained from the observation of these γ rays is their angles, which are essential for the angular correlation analysis.

B. Experiment B

The aim of experiment B was to extend the spectrum of high-spin resonances in ^{24}Mg to excitations above 22 MeV. To reach this energy region with good energy resolution, the α_0 particles had to be detected in forward direction. Because these high-lying states mostly decay through multiple-α emission, it was important to achieve suitable detector coverage of a significant fraction of the solid angle.

The experimental setup for experiment B consisted of three annular DSSDs, positioned in forward direction from the target, at 26, 73, and 237 mm distance, respectively. The last DSSD was located inside an annular ion chamber to provide particle identification through an energy loss measurement in isobutane gas at a pressure of 50 torr. It also contained an additional fourth DSSD which was used to identify particles punching through the main silicon detector. These detector systems supplied an essentially continuous coverage of the forward angles between 2.7° and 53° with respect to the beam axis.

This highly efficient setup also limited significantly the usable beam intensity, as the count rate was dominated by elastic scattering of beam particles and multiparticle breakup, as well as scattering from upstream beam collimators. Because of the large number of background reaction channels open, we focused our analysis on kinematically complete events, that is, events where all particles, including the heavy-ion residue, were detected and, thus, could be unambiguously identified through total energy and momentum conservation.

The silicon detectors were calibrated using a ^{228}Th α source. Because the calibration spectrum does not suitably cover the energy range of the typical α particles up to 40 MeV, the detector calibrations were improved using the experimental data. The original calibration was, however, sufficient to identify the decay path of most events unequivocally. Using such events, we fit the respective three- and four-body Q values, the total energy and momentum based on the known excitation and binding energies in ^{20}Ne by allowing the energy calibrations and detector positions to vary in a χ^2-minimization procedure. Applying these calibrations to the event analysis, we achieved a much improved resolution in the Q-value spectra. The deviation from the original calibrations remains small within the energy range covered by the calibration source. The fitted changes in detector positions correspond to a minor misalignment of the detectors with respect to the beam axis. This adopted detector geometry was tested and confirmed using elastic scattering events from the same data set.

During the experiment, twofold and higher particle coincidences were recorded. To achieve an unambiguous reaction channel selection, we analyzed the total momentum and energy for the three- and fourfold coincidence events and selected the ones matching the expected values for the $2\alpha + {}^{20}$Ne and $3\alpha + {}^{16}$O channels, respectively. Figure 2 provides the corresponding histogram of the total momentum in the center-of-mass (c.m.) frame and the total kinetic energy for quadruple-particle coincidence events analyzed under the $3\alpha + {}^{16}$O hypothesis.

The α particles of every event were sorted according to their respective energies in the beam-target center-of-mass frame, identifying the highest energy α particle as the α_0 particle,
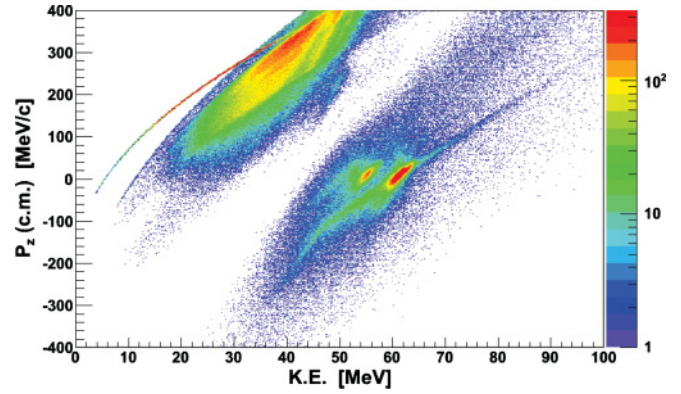

FIG. 2. (Color online) Experiment B. Histogram of events, displaying total z momentum (c.m.) vs total kinetic energy (lab system). The particle momenta analyzed are based on the $3\alpha + {}^{16}$O hypothesis. The events around KE = 60.7 MeV, Pz = 0 MeV/c were selected for further analysis.

emitted from the ^{28}Si compound state and the second and third as the α_1 and α_2 particles, respectively. The reconstruction of the excitation energy in ^{24}Mg, of the intermediate state in ^{20}Ne, and of the final state in ^{16}O were calculated through the two-body, three-body, and four-body Q values, respectively. A hypothetically exchanged assignment of α_0 and α_1, led to no discernible peaks in the ^{24}Mg excitation energy spectrum.

Figure 3 displays the spectrum of states in ^{20}Ne, populated in experiment B, reconstructed through the three- and four-body Q values. The spectrum from $2\alpha + {}^{20}$Ne events, displayed in Fig. 3(a), shows peaks at the bound-state energies of ^{20}Ne, namely the ground state, the 2_1^+ level at 1.63 MeV, and the 4_1^+ state at 4.25 MeV. In addition, weaker peaks are visible at higher energies, including the known ^{20}Ne states 2_1^- at 4.97 MeV, 4_1^- at 7.00 MeV, and 6_1^- at 10.61 MeV. The unique
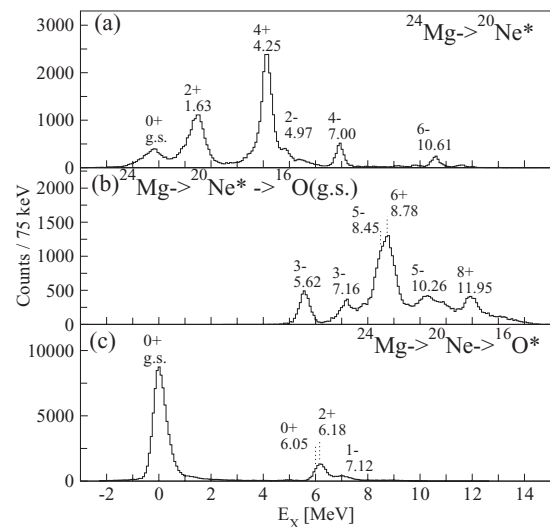

FIG. 3. Spectra of excited states observed in ^{20}Ne and ^{16}O with experiment B. (a) Spectrum of ^{20}Ne intermediate states for $2\alpha + {}^{20}$Ne events. (b) Spectrum of ^{20}Ne intermediate states for $3\alpha + {}^{16}$O events, gated on the ^{16}O ground state. (c) Spectrum of ^{16}O final states for $3\alpha + {}^{16}$O events.
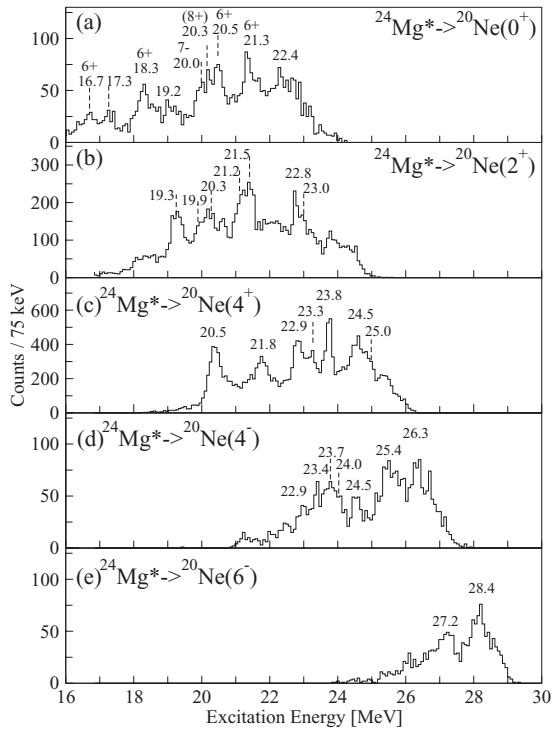
FIG. 4. Spectra of excited states observed in ^{24}Mg with experiment B, gated on α_1 decay toward the following ^{20}Ne states: (a) 0^+, (b) 2^+, (c) 4^+, (d) 4^-, (e) 6^-.

FIG. 5. Spectra of excited states observed in ^{24}Mg with experiment B, gated on their decay toward the 3^-, 5^-, and 6^+ states in ^{20}Ne and to the ground state of ^{16}O.

identification of $2\alpha + {}^{20}$Ne events establishes that these states decay by γ emission despite their location high above the α-decay threshold. These and other unnatural-parity states were also observed in Ref. [14] using the ^{12}C(^{12}C, α)^{20}Ne reaction.

Figure 3(b) displays the spectrum of intermediate ^{20}Ne states from $3\alpha + {}^{16}$O events, gated on the ^{16}O ground state. The largest peaks correspond to both the 5^-_1 and 6^+_1 states in ^{20}Ne, the former of which is indicated by a clear low-energy shoulder on the latter. Other ^{20}Ne levels, such as the $3^-_{1,2}$, the second 5^-, and the 8^+ states, are also observed. Figure 3(c) gives the spectrum of final ^{16}O states, with the ground state dominating the observed events.

In Fig. 4 the excitation energy spectra of ^{24}Mg from $2\alpha + {}^{20}$Ne events are displayed, gated on their decay toward the various ^{20}Ne states. A complex spectrum of excited states is observed, which will be compared to results from other experiments in Sec. V. The spectra contain events from excitation energies below 22.6 MeV, for which the α_0 particles are not stopped in the 500-μm-thick silicon detector. For these events, which included the signal of a punch-through detector, the kinematic reconstruction based on α_0 energies resulted in a degraded energy resolution. Therefore, below 22.6 MeV, the excitation energies were reconstructed using the α_1 energy and the final-state Q value. The consistency of both methods was tested for regular events. Level energies based on this alternative reconstruction method are assumed to have a systematic uncertainty of 100 keV, while the other level energies are determined with a 50-keV systematic uncertainty.

The spectra of states displayed in Fig. 4 were not analyzed further, because the associated γ radiation was not detected in
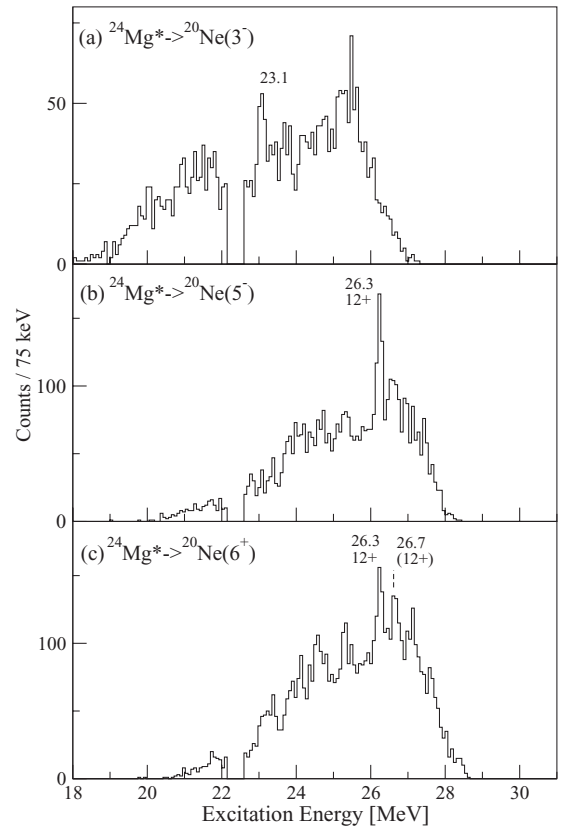
experiment B. The presence of ^{24}Mg states which decay toward the unnatural parity ^{20}Ne states is interesting [Figs. 4(d) and 4(e)]. It can be assumed that the associated structures represent high-spin states of unnatural parity in ^{24}Mg.

In Fig. 5 the ^{24}Mg excitation energy spectrum from $3\alpha + {}^{16}$O events is displayed, gated on the intermediate 3^-, 5^-, 6^+ states in ^{20}Ne. For these spectra, events around the DSSD punch-through excitation energy of 22.6 MeV are suppressed rather than reconstructed. For events gated on the 8^+ state in ^{20}Ne at 11.95 MeV, no resonant structure was observed.

III. ANGULAR CORRELATION FORMALISM FOR EMISSION OF MULTISTEP α AND γ CASCADES

In this section, we investigate the formalism to calculate and analyze angular correlations for a cascade of α particles and γ rays. The symbols and conventions follow Ref. [15]. The nucleus is produced in an excited state of unknown angular momentum I_1 and is aligned with $m_1 = 0$. The method to select an alignment axis for the I_1 state is discussed later in this section. The emission of the α_1 particle from the state I_1 will populate a state I_2, whose magnetic substate probabilities and correlations are represented as a density matrix $\rho_{m_2, m'_2}(I_2)$.

The particle cascades ($\alpha_1\gamma_2$, $\alpha_1\gamma_2\gamma_3$, or $\alpha_1\alpha_2$) emitted from I_1 will exhibit an angular correlation pattern determined by the coupling of their angular momenta to the intermediate and
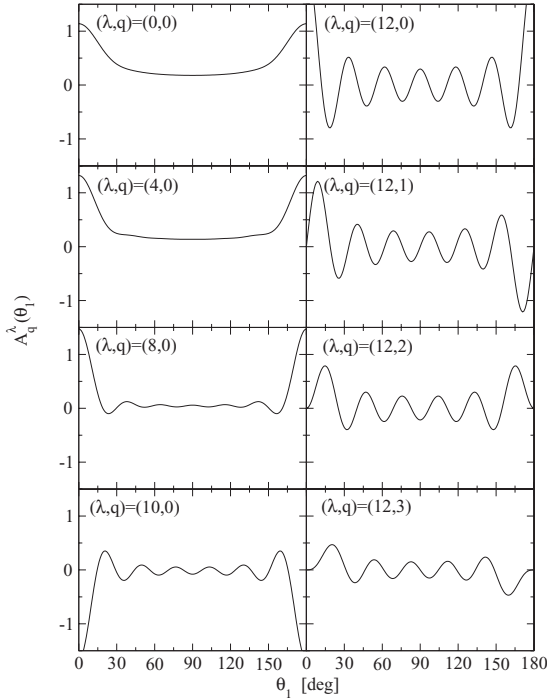
FIG. 6. Statistical tensor components [Eq. (1)] as functions of the angle for a $I_1 = 12 \longrightarrow I_2 = 6$ spin sequence.

final states. If multiple final magnetic substates are available, the angular correlations must be averaged over these. Here, we are interested in final states of angular momentum zero, where the magnetic projection m is unambiguously defined. The ensuing multiparticle angular correlations are an example of quantum entanglement, where the characteristic patterns disappear if any of the decay quanta remains undetected. In our analysis technique, the quantum numbers I_2, I_3, and I_4 are known and are used to analyze the experimental angular correlation pattern of α_1, which in turn determines the angular momentum I_1. We assume that the α_1 angular momentum takes the minimum value $L_1 = |I_1 - I_2|$, owing to the angular momentum barrier involved in α emission.

The density matrix after the first particle emission can be expressed in the m scheme [see Eq. (A2)], but for our analysis technique it is more useful to represent the same information through statistical tensors. The statistical tensor for the intermediate state I_2, populated after emission of the α_1 particle detected in the direction Ω_1, is given by the following expression (see Appendix Sec. II):

$$
\begin{aligned}
A_q^\lambda(I_1 \xrightarrow{\alpha_1} I_2)(\Omega_1) = (2\lambda + 1)^{1/2}(2I_1 + 1)\sum_{mm'}(-1)^{I_2+m'} \\
\times \begin{pmatrix} I_2 & I_2 & \lambda \\ m & m' & q \end{pmatrix}\begin{pmatrix} I_2 & L & I_1 \\ m & -m & 0 \end{pmatrix} \\
\times \begin{pmatrix} I_2 & L & I_1 \\ m' & -m' & 0 \end{pmatrix} Y_{-m}^L(\Omega_1)\left(Y_{-m'}^L\right)^*(\Omega_1).
\end{aligned}
\tag{1}
$$

A set of statistical tensor functions for the $12 \to I_2 = 6$ spin sequence is displayed in Fig. 6. The rank λ of the statistical

tensor and the associated q index represent the degree of orientation in the ensemble of nuclei, which also determines the symmetry of the subsequent radiation distribution. The rank λ runs between zero and $2I_2$, while q runs between $-\lambda$ and λ. An isotropic ensemble only possesses the A_0^0 term. For ensembles with cylindrical symmetry, only the $q = 0$ terms are nonzero. Expression (1) does not produce odd values of λ, which would represent an asymmetry with respect to a reversal of the z axis. For all the conditions considered in this paper, strongly aligned ensembles are present, which possess terms in all A_q^λ up to the maximum allowed value $\lambda = 2I_2$. The statistical tensor components of the maximally allowed λ and lowest $|q|$ contain the characteristic patterns used to determine spin and parity.

Following the population of the I_2 state, with its alignment pattern represented by the A_q^λ statistical tensor, we now analyze the angular correlation of α_2, γ_2 or the two-step $\gamma_2\gamma_3$ emission, respectively. In all cases the final state will have zero angular momentum and, thus, only $m = 0$.

A. Angular correlations with a second α particle

The angular correlation expression for the α_2 emission from the I_2 state, represented through its statistical tensor, follows the time-reversed expression of Eq. (1):

$$
B_q^\lambda(I_2 \xrightarrow{\alpha} I_3)(\Omega) = (-1)^{\lambda-q} A_{-q}^\lambda(I_3 \xrightarrow{\alpha} I_2)(\Omega). \tag{2}
$$

As derived in the Appendix in the discussion leading up to Eq. (A8), the B_q^λ can be reduced to an expression proportional to a single spherical harmonic, if $I_3 = 0$:

$$
B_q^\lambda(I_2 \xrightarrow{\alpha_2} 0)(\Omega_2) = \frac{(-1)^{I_2+q}}{\sqrt{4\pi}}\begin{pmatrix} I_2 & I_2 & \lambda \\ 0 & 0 & 0 \end{pmatrix} Y_q^\lambda(\Omega_2). \tag{3}
$$

The angular correlation expression for both α particles is obtained by folding the A_q^λ and B_q^λ expressions over the indices λ, q using the appropriate normalization:

$$
\begin{aligned}
W_{\alpha\alpha}(\Omega_1, \Omega_2) = \sum_{\lambda,q}(2I_2 + 1)A_q^\lambda(I_1 \xrightarrow{\alpha_1} I_2)(\Omega_1) \\
\times B_q^\lambda(I_2 \xrightarrow{\alpha_2} 0)(\Omega_2). \tag{4}
\end{aligned}
$$

Because the initial and final states are populated in pure $m = 0$ substates and, thus, represent cylindrically symmetric ensembles, we have the freedom to rotate the coordinate frame to choose the ϕ_1 angle to be zero. This choice allows us to only consider real values for A_q^λ and B_q^λ. Furthermore, positive and negative values of q differ only by a sign change in both terms, so that only values $q \geqslant 0$ need to be included in the sum with an appropriate weight.

The principle of our data analysis technique is suggested by the structure of Eq. (4), which factorizes in two terms, $A_q^\lambda(\theta_1)$ expressing the dependence on the α_1 angles and $B_q^\lambda(\Omega_2)$ expressing the dependence on the angles of the second particle. The set of $B_q^\lambda(\Omega_2)$ tensor components form a basis in their angular space, which, being proportional to a single spherical harmonic function, is orthogonal in the indices λ and q. This allows one to represent the experimental correlation distribution $w(\theta_1, \Omega_2)$ as a set of basis coefficients

$a_q^\lambda(\theta_1)$ with respect to the orthogonal basis $B_q^\lambda(\Omega_2)$. Here and in the following discussions, the basis representations of experimental data are denoted by small letter symbols. For an ideal detector system with perfectly isotropic detection efficiency, the basis coefficients $a_q^\lambda(\theta_1)$ can be obtained by folding the experimental data with the normalized basis functions through

$$a_q^\lambda(\theta_1) = \int d\Omega_2 \, w(\theta_1, \Omega_2) \frac{B_q^\lambda(\Omega_2)}{||B_q^\lambda||}. \tag{5}$$

These $a_q^\lambda(\theta_1)$ coefficients will be compared to the $A_q^\lambda(\theta_1)$ ones of Eq. (1) to assign spins to the initial state of the decay cascade. The practical value of representing the experimental data this way lies in the fact that only a few basis coefficients contain the relevant information, namely the correlations corresponding to the maximum λ value allowed for the intermediate state I_2 and the lowest three values $q = 0, 1, 2$. The implementation of this technique with respect to data sorting, error calculations, and corrections for nonuniform detector responses is described in Sec. IV.

B. Angular correlations with a γ photon

The angular correlations for the emission of one γ ray from the nonaxially oriented state I_2 is described by expression 12.186 of Ref. [15]:

$$B_q^\lambda(I_2 \xrightarrow{\gamma_2} 0)(\Omega_2) = (2\lambda + 1)^{-1/2} F_\lambda(\gamma) Y_q^\lambda(\Omega_2), \tag{6}$$

where the well-known F coefficients of γ radiation [15,16] are used. Again, the angular correlation pattern is calculated by folding the expressions of Eqs. (1) and (6) over λ and q:

$$W_{\alpha\gamma}(\Omega_1, \Omega_2) = \sum_{\lambda,q}(2I_2 + 1)A_q^\lambda(I_1 \xrightarrow{\alpha_1} I_2)(\Omega_1)$$
$$\times B_q^\lambda(I_2 \xrightarrow{\gamma_2} 0)(\Omega_2). \tag{7}$$

The data analysis will be performed in complete analogy to the case of α-α correlations described in Eq. (5).

C. Angular correlations with a γ-γ cascade

The angular correlation pattern for a cascade of two γ rays emitted from a nonaxially oriented state such as I_2, is derived as expression 12.204 in Ref. [15]:

$$B_q^\lambda(I_2 \xrightarrow{\gamma_2} I_3 \xrightarrow{\gamma_3} 0)(\Omega_2, \Omega_3)$$
$$= \sum_{\lambda_2\lambda_1 q_2 q_1}(2\lambda_2 + 1)^{-1/2} F_{\lambda_1}^{\lambda_2,\lambda}(\gamma_2) F_{\lambda_2}(\gamma_3)$$
$$\times \begin{pmatrix} \lambda & \lambda_1 & \lambda_2 \\ q & q_1 & q_2 \end{pmatrix} Y_{q_1}^{\lambda_1}(\Omega_2) Y_{q_2}^{\lambda_2}(\Omega_3). \tag{8}$$

The angular correlation distribution of $\alpha_1\gamma_2\gamma_3$ cascades can thus be calculated as

$$W_{\alpha\gamma\gamma}(\Omega_1\Omega_2\Omega_3) = \sum_{\lambda,q}(2I_2 + 1)A_q^\lambda(I_1 \xrightarrow{\alpha_1} I_2)(\Omega_1)$$
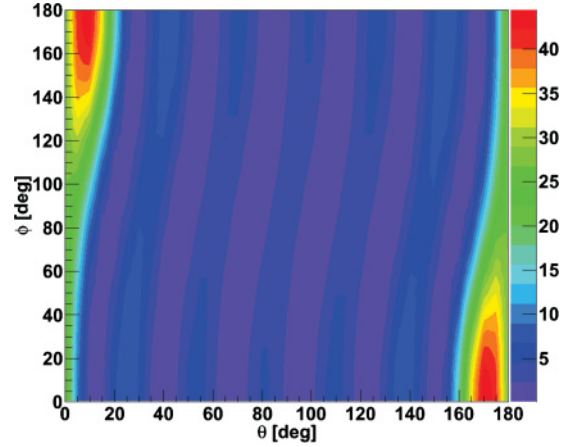$$\times B_q^\lambda(I_2 \xrightarrow{\gamma_2} I_3 \xrightarrow{\gamma_3} 0)(\Omega_2, \Omega_3). \tag{9}$$

FIG. 7. (Color online) Calculated angular distribution of α_1 particle emitted in cascade with an α_0 particle at the fixed angle $\theta = 10°\phi = 0°$ in the spin sequence $12 \to 6 \to 0$ (see text for details).

The data analysis through basis expansion follows the same principle as described for the case of $\alpha_1\alpha_2$ correlations. Again, the B_q^λ patterns form an orthogonal basis, but, in this case, of the combined two-particle angular space of γ_2 and γ_3. In complete analogy to the previous cases, the basis representation of the experimental data is obtained through

$$a_q^\lambda(\theta_1) = \int d\Omega_2 d\Omega_3 \, w(\theta_1, \Omega_2, \Omega_3) \frac{B_q^\lambda(\Omega_2, \Omega_3)}{||B_q^\lambda||}. \tag{10}$$

D. Dynamic alignment axis and coordinate systems

The angular correlation analysis we are describing relies on the preparation of an excited state of ^{24}Mg with unknown angular momentum, but with magnetic quantum number $m = 0$. The ^{28}Si compound states will automatically have $m = 0$, owing to the fact that the orbital angular momentum is aligned perpendicular to the beam axis and both beam and target nuclei are spin = 0 particles. In our experiments, we detected the α_0 particles at small angles relative to the beam axis (smaller than $\approx 20°$), which nevertheless introduces components of $m = 1$ to the wave function of the ^{24}Mg state.

This problem was solved by finding a quasiclassical approximation to the effects of the α_0 emission on the subsequent particle angles. In the cases studied here, one can find a new alignment axis for which $m' = 0$ and toward which all subsequent particle angles are referenced. The orientation of this axis depends on the angular momentum and specific detection angles of the α_0 particle. Our analysis is equivalent to the method applied in studies of ^{12}C + ^{12}C breakup in Refs. [17,18] and of α angular distributions in Ref. [19].

The direction of the alignment axis can be calculated using the α-α correlation formalism described in this paper. In Fig. 7, we are displaying the angular correlation pattern calculated for two α particles in a cascade $12^+ \to 6^+ \to 0^+$, with the first particle at a fixed direction $\theta_0 = 10°$, $\phi_0 = 0°$. This pattern can be simplified by introducing a new, tilted alignment axis, which lies in the plane of α_0 emission, on the opposite side. With respect to this axis, the angular distribution

approximates the squared sixth-order Legendre polynomial $P_6[\cos(\theta')]$, expected for emission from a 6^+ state with $m' = 0$. Our calculations indicate that the angle of the new alignment axis in the original frame can be taken as $\theta_{\text{tilt}} = \theta_0 L(\alpha_0)/I_1$, consistent with the prescription given in Refs. [17–19].

During the analysis of angular distribution and correlation patterns in our experiments, we tested a range of hypothetical values for $L(\alpha_0)/I_1$. The particular hypothesis was applied event by event, using the detected α_0 angle to calculate an alignment axis toward which all subsequent particle angles were referenced.

The angles of α emission relevant for the angular correlation analysis are determined in the center-of-mass system of the nucleus, whose angular momentum is represented in their decay wave functions. For instance, to reconstruct the angular momentum of a ^{24}Mg state, the emission angle of α_1 is analyzed in the ^{24}Mg frame of reference while the angles of α_2 particles are analyzed in the ^{20}Ne frame of reference. The dynamic alignment axis described above is implemented through a coordinate rotation in the ^{24}Mg coordinate system, which then is transmitted through Lorentz transformations to the subsequent reference frames.

IV. ANALYSIS OF MULTIPARTICLE ANGULAR CORRELATIONS USING AN ORTHOGONAL BASIS TRANSFORMATION

In this section, we address the data analysis method applied to the present experiments, which used the expansion of the experimental correlation data into coefficients of an orthogonal basis. We also describe the data sorting and error calculations as well as the corrections for the nonisotropy of the detector systems.

A. Angular correlation analysis for experiment A: α_1-γ_2 correlations

The geometry and energy dependence of the detector acceptance is expressed as a product of the α-detector acceptance $\epsilon_1(\theta_1)$ and the γ-detection efficiency $\epsilon_2(\Omega_2)$. The acceptance ϵ_1 was calculated using a Monte Carlo simulation of the reaction kinematics, while the efficiency ϵ_2 was measured using standard γ-calibration sources.

While the α_1-detector acceptance can be applied directly to the experimental data, the effect of angular biases in the detection of γ_2 enters by creating nonorthogonalities of the basis functions. Because the effects remain small, we chose to apply corrections to the theoretical hypothesis rather than to the experimental data. Before we discuss this effect of detector acceptance in the following paragraphs, we describe the practical implementation of the data analysis, the error calculations, and normalizations.

The folding integral of the experimental data $w(\theta_1, \Omega_2)$ with the basis vectors $B_q^\lambda(\Omega_2)$ is performed through

$$a_q^\lambda(\theta_1) = \frac{1}{\epsilon_1(\theta_1)} \int d\Omega_2 w(\theta_1, \Omega_2) \frac{B_q^\lambda(\Omega_2)}{||B_q^\lambda||}$$

$$= \frac{1}{\epsilon_1(\theta_1)} \sum_{j=\text{det.}} w(\theta_1, \Omega_2[j]) \frac{B_q^\lambda(\Omega_2[j])}{||B_q^\lambda||} \quad (11)$$

$$= \frac{1}{\epsilon_1(\theta_1)} \sum_{i=\text{evt.}} \frac{B_q^\lambda(\Omega_2[i])}{||B_q^\lambda||}. \quad (12)$$

In this expression, we made use of the fact that all detector systems of Gammasphere [13] cover the same fraction of the total solid angle, so that the integral over the Ω_2 space can be replaced in Eq. (11) by the sum over the events from the respective detectors. Furthermore, because every event at a given angle Ω_2 enters the calculations of a_q^λ with the same weight $B_q^\lambda(\Omega_2)/||B_q^\lambda||$, the summation of events and the summation over the detectors can be interchanged. This allows us to accumulate the histograms a_q^λ event by event, incrementing by the value $B_q^\lambda[\Omega_2[i]]/||B_q^\lambda||$, using the angle $\Omega_2(i)$ of the specific event i, as expressed in Eq. (12). Naturally, the a_q^λ histograms are represented as floating point values during the data analysis.

The normalization factor in Eq. (11) is calculated as the rms value of the basis function, averaged over the M detectors in the specific setup, with the goal to apply an average weight of 1 to the events of the experiment:

$$\left\| B_q^\lambda \right\| = \sqrt{1/M \sum_{j=\text{det.}} \left(B_q^\lambda(\Omega_2[J]) \right)^2}. \quad (13)$$

The uncertainties of the transformed patterns a_q^λ are calculated by first-order error propagation applied to Eq. (11), where only the statistical uncertainties of the experimental counts $\Delta w(\theta_1, \Omega_2) = \sqrt{w(\theta_1, \Omega_2)}$ are considered:

$$\Delta a_q^\lambda(\theta_1) = \frac{1}{\epsilon_1(\theta_1)} \frac{1}{||B_q^\lambda||} \sqrt{\sum_{j=\text{det.}} (\Delta w(\theta_1, \Omega_2[j]))^2 \left(B_q^\lambda(\Omega_2[j]) \right)^2}$$

$$= \frac{1}{\epsilon_1(\theta_1)} \frac{1}{||B_q^\lambda||} \sqrt{\sum_{i=\text{evt.}} \left(B_q^\lambda(\Omega_2[i]) \right)^2}. \quad (14)$$

In this context, the normalization prescription of Eq. (13) ensures that the uncertainties of all basis coefficients a_q^λ are approximately the same for different values of λ and q. The error calculations of Eq. (14) are performed by incrementing error histograms in parallel with sorting the a_q^λ histograms.

The Gammasphere spectrometer used in experiment A constitutes an almost ideal 4π-detector system with very small angular biases. This makes it well suited for the present analysis method. Nevertheless, variations in the efficiency of the detector systems and missing detectors create small biases in the angular coverage and thus lead to nonorthogonal components in the efficiency-weighted basis B_q^λ, slightly distorting the extracted patterns a_q^λ.

We calculate this effect by applying the calibrated experimental response to an ideal theoretical correlation pattern,

$$\tilde{W}(\theta_1, \Omega_2) = \epsilon_1(\theta_1) \sum_{\lambda,q} (2I_2 + 1) A_q^\lambda(\theta_1) \epsilon_2(\Omega_2) B_q^\lambda(\Omega_2), \quad (15)$$

and by analyzing this pattern through the transformation of Eq. (11) as if it constituted experimentally observed data. This analysis leads to a modified hypothetical pattern $\tilde{A}_q^\lambda$, which is, nevertheless, very similar to the ideal A_q^λ coefficients of the

correlation theory:

$$\tilde{A}_q^\lambda = \frac{1}{\epsilon(\theta_1)} \sum_{j=\text{det.}} \tilde{W}(\theta_1, \Omega_2) \frac{B_q^\lambda(\Omega_2[j])}{||B_q^\lambda||}$$

$$= (2I_2 + 1) \sum_{j=\text{det.}} \sum_{\lambda', q'} A_{q'}^{\lambda'}(\theta_1) \epsilon_2(\Omega_2) B_{q'}^{\lambda'}(\Omega_2[j]) \frac{B_q^\lambda(\Omega_2[j])}{||B_q^\lambda||}$$

$$= (2I_2 + 1) \sum_{\lambda' q'} \epsilon_{\lambda, q}^{\lambda', q'} A_{q'}^{\lambda'}(\theta_1). \tag{16}$$

Here, we have introduced the response matrix

$$\epsilon_{\lambda, q}^{\lambda', q'} = \sum_{j=\text{det.}} \epsilon_2(\Omega_2[j]) B_{q'}^{\lambda'}(\Omega_2[j]) \frac{B_q^\lambda(\Omega_2[j])}{||B_q^\lambda||}. \tag{17}$$

Equation (16) shows the modification of the theoretical A_q^λ coefficients through the effects of a nonisotropic detector system, as expressed in the response matrix. With the $\epsilon_2(\Omega_2)$ efficiency obtained from calibrations, the off-diagonal elements of this matrix are smaller than 30% and do not lead to a significant distortion of the $A_q^\lambda(\theta_1)$ shapes. The effects are, nevertheless, important to achieve a quantitative agreement between the experiment and the correlation hypothesis.

We analyzed the $\alpha_0 \alpha_1 \gamma_2$ coincidence events from experiment A and selected the $^{24}\text{Mg} \xrightarrow{\alpha_1} {}^{20}\text{Ne}(2^+) \xrightarrow{\gamma_2} {}^{20}\text{Ne}(0^+)$ decay path by gating on the three-body Q-value parameter corresponding to the $^{20}\text{Ne}(2^+)$ state and the γ transition energy of 1.368 MeV.

For these events, we extracted the angular correlation patterns according to the method outlined above, sorting the data into two-dimensional histograms $a_q^\lambda(Q_2, \theta_1)$ with the ^{24}Mg excitation energy and the θ_1 angle on the two axes. The spectra for $(\lambda, q) = (4, 0), (4, 1), (4, 2)$ were analyzed, corresponding to the maximum λ value present in the statistical tensor of the 2^+ intermediate state. We sorted six sets of these histograms, corresponding to different hypotheses for the $L(\alpha_0)/I_1 = (0.3, 0.5, 0.7, 0.9, 1.2, 1.5)$, which are applied during the data sorting, according to the dynamic alignment axis correction described in Sec. III D.

Through background subtraction and gating on the peaks in the excitation energy spectrum, we obtained the associated angular correlation patterns. We consistently found that the maximum amplitude in the correlation pattern was observed for values corresponding to $I_0 = 15$–17. We corrected the angular distribution values in θ_1 with the detector acceptance $\epsilon_1(\theta_1)$ obtained from a Monte Carlo simulation and compared this pattern with the orthogonality-corrected hypothetical correlation pattern [Eq. (16)] calculated for various I_1 hypotheses.

Figures 8 and 9 provide examples of such analysis for the 15.10- and 16.53-MeV peaks, establishing them as the 7_2^- and 8_4^+ states, respectively. The correlation patterns for $(\lambda, q) = (4, 0)$ exhibit clearly the effect of the detector acceptance correction applied to the hypothetical patterns: While the uncorrected A_0^4 patterns show oscillations around zero, the experimental and acceptance-corrected hypothetical ones are offset toward positive values, owing to an overlap between the efficiency-weighted B_0^4 and B_0^0 basis vectors. This effect represents the only significant distortion to the data because of
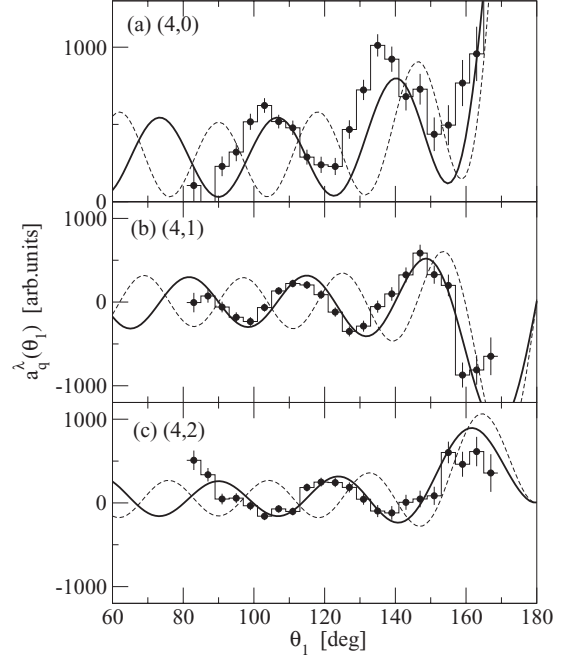

FIG. 8. Angular correlation pattern observed for the 15.10-MeV 7^- state. The data are reproduced from Ref. [11]. Plotted are the experimental distributions $a_q^\lambda(\theta_1)$ compared to the $\tilde{A}(\theta_1)$ curves, calculated for the spin hypotheses $I_1^\pi = 7^-$ (solid line) and 8^+ (dashed line). Panels (a), (b), and (c) display the experiment and hypothetical data for $(\lambda, q) = (4, 0), (4, 1),$ and $(4, 2)$, respectively.

geometrical biases in the detection system and does not change the characteristic angular oscillations of the patterns.

B. Angular correlation analysis for experiment A: $\alpha_1 \gamma_2 \gamma_3$ correlations

For states predominantly decaying toward the 4^+ level of ^{20}Ne, we have to analyze the correlation between all three particles $\alpha_1 \gamma_2 \gamma_3$ to follow the decay cascades to the final 0^+ state and determine the initial angular momenta. Although an additional γ photon with its respective angles has to be considered, the analysis is completely analogous to the procedure described previously. In this case, the experimental angular correlation pattern $w(\theta_1, \Omega_2, \Omega_3)$ is analyzed with respect to the $B_q^\lambda(\Omega_2, \Omega_3)$ tensor of Eq. (8). Because $I_2 = 4$, the maximum rank of the orientation tensor is $\lambda = 8$

$$a_q^\lambda(\theta_1) = \frac{1}{\epsilon_1(\theta_1)} \int d\Omega_2 d\Omega_3 w(\theta_1, \Omega_2, \Omega_3) \frac{B_q^\lambda(\Omega_2, \Omega_3)}{||B_q^\lambda||}$$

$$= \sum_{j=\text{det.pairs}} w(\theta_1, \Omega_2[j], \Omega_3[j]) \frac{B_q^\lambda(\Omega_2[j], \Omega_3[j])}{||B_q^\lambda||}$$

$$= \sum_{i=\text{events}} \frac{B_q^\lambda(\Omega_2[i], \Omega_3[i])}{||B_q^\lambda||}. \tag{18}$$

Again, this experimental pattern is compared to an hypothetical one, corrected for the detector responses

$$\tilde{A}_q^\lambda(\theta_1) = (2I_2 + 1) \sum \epsilon_{\lambda, q}^{\lambda', q'} A_{q'}^{\lambda'}(\theta_1), \tag{19}$$
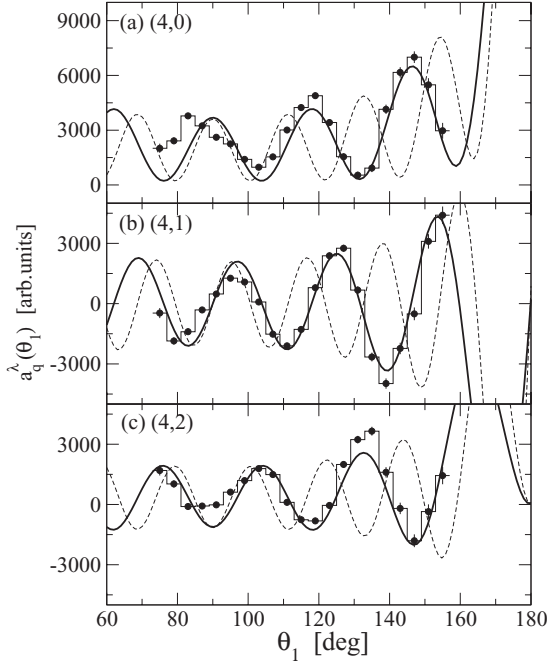
FIG. 9. Angular correlation pattern observed for the 16.54-MeV 8^+ state. The data are reproduced from Ref. [11]. Plotted are the experimental distributions $a_q^\lambda(\theta_1)$ compared to the $\tilde{A}(\theta_1)$ curves, calculated for the spin hypotheses $I_1^\pi = 8^+$ (solid line) and 10^+ (dashed line). Panels (a), (b), and (c) display the experiment and hypothetical data for $(\lambda, q) = (4, 0)$, $(4, 1)$, and $(4, 2)$, respectively.
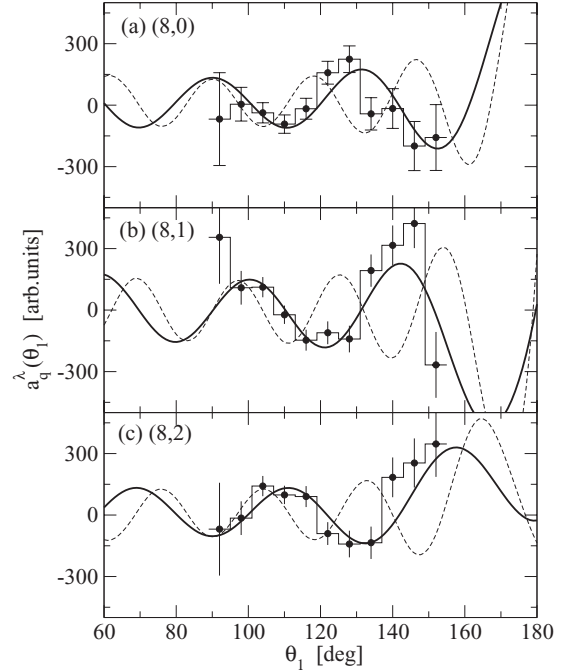

FIG. 10. Angular correlation pattern observed for the 17.22-MeV 8^+ state. The data are reproduced from Ref. [11]. Plotted are the experimental distributions $a_q^\lambda(\theta_1)$ compared to the $\tilde{A}(\theta_1)$ curves, calculated for the spin hypotheses $I_1^\pi = 8^+$ (solid line) and 10^+ (dashed line). Panels (a), (b), and (c) display the experiment and hypothetical data for $(\lambda, q) = (8, 0)$, $(8,1)$, and $(8, 2)$, respectively.

with the response matrix

$$\epsilon_{\lambda,q}^{\lambda',q'} = \sum_{j=\text{det.pairs}} \epsilon_{23}(\Omega_2[j], \Omega_3[j])$$
$$\times B_{q'}^{\lambda'}(\Omega_2[j], \Omega_3[j]) \frac{B_q^\lambda(\Omega_2[j], \Omega_3[j])}{||B_q^\lambda||}, \quad (20)$$

which is calculated from the coincidence efficiency $\epsilon_{23}(\Omega_2, \Omega_3)$ of the detector pairs in Gammasphere.

We selected the $\alpha_0 \alpha_1 \gamma_2 \gamma_3$ events corresponding to the ^{24}Mg $\xrightarrow{\alpha_1}$ ^{20}Ne(4^+) $\xrightarrow{\gamma_2 \gamma_3}$ ^{20}Ne(0^+) decay path by gating on the three-body Q-value parameter corresponding to the ^{20}Ne(4^+) level and the coincident γ transitions of 1.368 and 1.613 MeV energy. For these events, the angular correlation data were analyzed by sorting the $a_q^\lambda(\theta_1)$ histograms for $(\lambda, q) = (8, 0), (8, 1), (8, 2)$, each for six hypotheses of the $L(\alpha_0)/I_1$ parameter, with values of (0.3, 0.5, 0.7, 0.9, 1.2, 1.5).

We created background-subtracted a_q^λ spectra for the peaks in the corresponding excitation energy spectrum. Two examples are displayed in Figs. 10 and 11. The distributions establish the 17.22-MeV state as $I^\pi = 8_5^+$ and the 19.21-MeV level as $I^\pi = 10_1^+$, a result published previously in Ref. [12].

C. Angular correlation analysis for experiment B: α_1-α_2 correlations

Before continuing with the $\alpha_1 \alpha_2$ angular correlation analysis for the data from experiment B, we analyzed the angular distributions of α_1 particles populating the 0^+ ground

state of ^{20}Ne as a simpler case. We sorted sets of the histograms corresponding to different hypotheses for the $L(\alpha_0)$ value involved in the dynamic alignment axis described in Sec. III D, varying values of $L(\alpha_0)/I_1$ between 0.1 and 1.0. All angular distribution and correlation patterns observed in this experiment and described hereafter are consistent with an initial angular momentum I_0 of 15 or 16. Examples of the background-subtracted angular distributions observed in experiment B are displayed in Fig. 12. They are consistent with a similar experiment performed by Kelly *et al.* [19].

The $\alpha_1 \alpha_2$ angular correlation analysis for experiment B is performed in analogy to the methods described above. The detection efficiency was calculated through a Monte Carlo simulation of the detector geometry as a function of the reaction Q value. It is factorized as $\epsilon_1(\theta_1) \epsilon_2(\Omega_2)$, which in this case becomes an approximation, as the α_1 emission direction influences to some degree the angular acceptance for α_2.

In the events of experiment B, the angular coordinates of the second particle are continuous and not associated with individual detectors. Therefore, the basis normalization and acceptance correction were calculated from integrals rather than sums as

$$||B_q^\lambda|| = \sqrt{\int d\Omega_2 \epsilon_2(\Omega_2) \left\{ B_q^\lambda(\Omega_2) \right\}^2} \quad (21)$$

and

$$\epsilon_{\lambda,q}^{\lambda',q'} = \int d\Omega_2 \epsilon_2(\Omega_2) B_{q'}^{\lambda'}(\Omega_2) \frac{B_q^\lambda(\Omega_2)}{||B_q^\lambda||}. \quad (22)$$
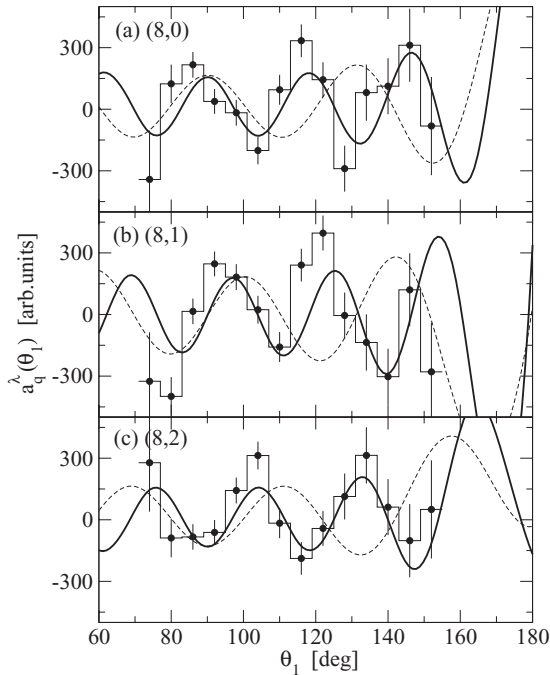
FIG. 11. Angular correlation pattern observed for the 19.21-MeV 10^+ state. The data are reproduced from Ref. [12]. Plotted are the experimental distributions $a_q^\lambda(\theta_1)$ compared to the $\tilde{A}(\theta_1)$ curves, calculated for the spin hypotheses $I_1^\pi = 10^+$ (solid line) and 8^+ (dashed line). Panels (a), (b), and (c) display the experiment and hypothetical data for $(\lambda, q) = (8, 0)$, (8,1), and (8, 2), respectively.

FIG. 12. Angular distribution pattern observed for various states decaying toward the ^{20}Ne ground state.

Owing to the limited coverage in Ω_2 angles, the nondiagonal terms of the response matrix $\epsilon_{\lambda,q}^{\lambda',q'}$ are larger than in the previous cases and reach up to 50%. Nevertheless, the shapes of the $\tilde{A}_q^\lambda$ curves are only mildly distorted, as visible in the analysis presented in Figs. 13 and 14.

With these expressions, the data transformation was performed in complete analogy to Eq. (12) and the hypotheses are calculated through Eq. (16). The basis transformation was applied to the angular correlations of α_1 and α_2 detected in experiment B. We selected the $\alpha_0 \alpha_1 \alpha_2$ events corresponding to the $^{24}\text{Mg} \xrightarrow{\alpha_1} {}^{20}\text{Ne}(5^-) \xrightarrow{\alpha_2} {}^{16}\text{O}(0^+)$ and $^{24}\text{Mg} \xrightarrow{\alpha_1} {}^{20}\text{Ne}(6^+) \xrightarrow{\alpha_2} {}^{16}\text{O}(0^+)$ decay paths by gating on the three-body Q-value parameter corresponding to the intermediate ^{20}Ne states and the particle identification gates described in Sec. II B.

We selected events where α_0 was detected in the most forward annular detector, limiting the laboratory angles to $\theta_0 < 20°$, which allows us to apply the dynamic alignment axis correction described in Sec. III D.

Figure 13 provides the angular correlations of the 26.28-MeV excited state in ^{24}Mg, observed through its $\alpha_1 \alpha_2$ decay cascade leading to the 5^- state of ^{20}Ne and the ground state of ^{16}O. In the figure, the observed correlation spectrum is compared with the pattern calculated for a 12^+ and a 10^+ hypothesis, using the $\lambda = 10$ statistical tensor components. The assignment of 12^+ to the 26.28-MeV state is based on a $\chi^2 = 0.81$ value, while 11^- and 10^+ hypotheses lead to $\chi^2 = 1.62$ and $\chi^2 = 2.0$, respectively. While the χ^2 values alone are at the limit of statistical significance, it should
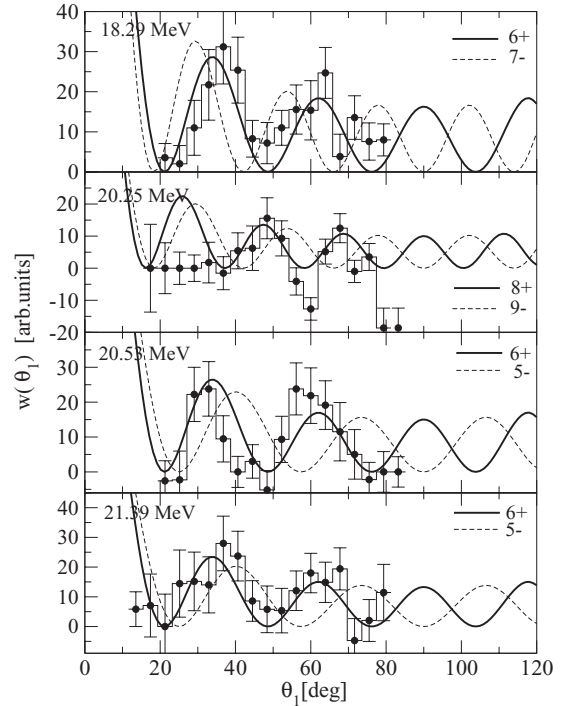
be noted that the correlation patterns exhibit the expected periodic character, which cannot be matched unless $L = 7$ is adopted.

The 26.28-MeV state also has a decay branch to the 6^+ state. The corresponding angular correlations were analyzed using the $\lambda = 12$ statistical tensor components. The correlation patterns, displayed in Fig. 14, also fit a 12^+ hypothesis at a level of $\chi^2 = 1.41$ vs the 11^- and 10^+ hypotheses at $\chi^2 = 2.89$ and $\chi^2 = 2.11$, respectively. The 12^+ assignment confirms that both decay branches originate from the same excited state.

The identification of a 12^+ level is the most prominent result from experiment B. Whether this state represents the lowest 12^+ level in ^{24}Mg is an important question which, owing to the limited statistics of experiment B, cannot yet be answered conclusively. At least two more states at lower energy (at 24.60 and 25.40 MeV) were observed, but could not be assigned spins. Another state at 26.67 MeV is tentatively identified as (12^+) through its decay toward the 6^+ level.

V. RESULTS AND DISCUSSION

The combined data from experiments A and B establish a more complete spectrum of high-spin excitations in ^{24}Mg, providing unambiguous spin and parity quantum numbers to 20 excited states belonging to the complex spectrum of high-spin resonances in the continuum. Nevertheless, it remains a difficult undertaking to establish a complete set of states. The resonant nature of the excitation function for the ^{24}Mg high-spin states leads to difficulties comparing the spectra of experiments with different beam energies. The
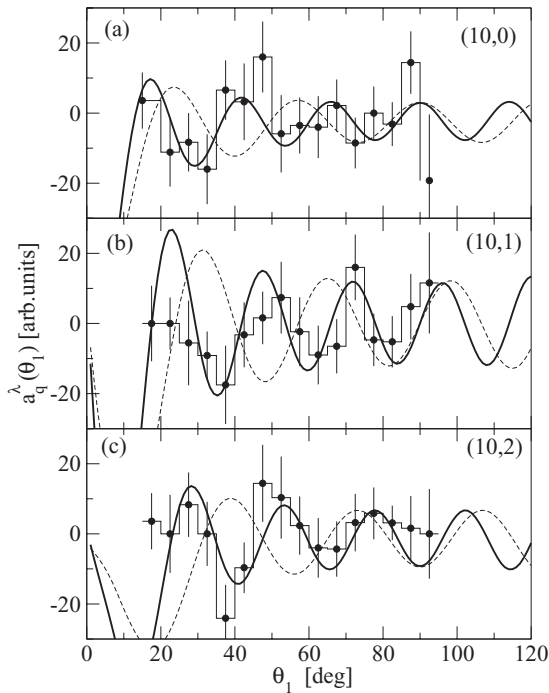
FIG. 13. Angular correlation pattern observed for the 26.3-MeV 12^+ state, analyzed through its sequential α decay toward ^{20}Ne(5^-) and ^{16}O(0^+). Plotted are the experimental distributions $a_q^\lambda(\theta_1)$ compared to the $A(\tilde{\theta}_1)$ curves, for the spin hypotheses $I_1^\pi = 12^+$ (solid line) and 10^+ (dashed line). The different panels display the experimental and hypothetical $\tilde{A}_q^\lambda$ distributions for $(\lambda, q) = (10, 0)$, (10,1), and (10, 2), in panels (a), (b), and (c), respectively.

FIG. 14. Angular correlation pattern observed for the 26.3-MeV 12^+ state, analyzed through its sequential α decay toward ^{20}Ne(6^+) and ^{16}O(0^+). Plotted are the experimental distributions $a_q^\lambda(\theta_1)$ compared to $A(\tilde{\theta}_1)$ for the spin hypotheses $I_1^\pi = 12^+$ (solid) and 10^+ (dashed). The different panels display the experimental and hypothetical $\tilde{A}_q^\lambda$ for $(\lambda, q) = (12, 0)$, (12,1), and (12, 2), in panels a,b and c, respectively.

results from experiment A and B are summarized in Tables I and II, respectively. They are placed in the context of known excitations, represented by Refs. [11,12,19–21].

The spectrum of states observed in both experiments indicates that most states with known spin exhibit a single dominant α-decay branch toward only one ^{20}Ne state. In our data, there are only two firmly established exceptions: the 8^+ state at 14.150 MeV, with both the $L = 8$ and the $L = 6$ decay analyzed, and the new 12^+ state at 26.28 MeV, with $L = 6$ and $L = 7$ α decays observed and analyzed.

A particularly challenging part of the spectrum is located around 16.5 MeV excitation. A triplet of states is reported in Ref. [20], at 16.29, 16.60, and 16.92 MeV. Zurmühle *et al.* [8] found a doublet of states at 16.30 and 16.84 MeV, assigned spin $8^+, 9^-$ and decaying toward the ^{20}Ne 2^+ state. In experiment A, we observe only one 8^+ state at 16.54 MeV. This peak is the dominant one in the spectrum of this measurement. It also appears as the strongest peak in the corresponding spectrum of Ref. [19]. Because of its dominance at the beam energy of experiment A, it is likely that the neighboring 16.30- and 16.84-MeV peaks were not observable.

The discovery of the lowest 10^+ state at 19.07 MeV was the most prominent result of experiment A, published in Ref. [11]. This state, decaying predominantly by α emission to the 4^+ level of ^{20}Ne, also has a weak γ branch toward the rotational 8_2^+ state at 13.212 MeV. This observation established the level as a member of the lowest rotational band. Energetically, it lies
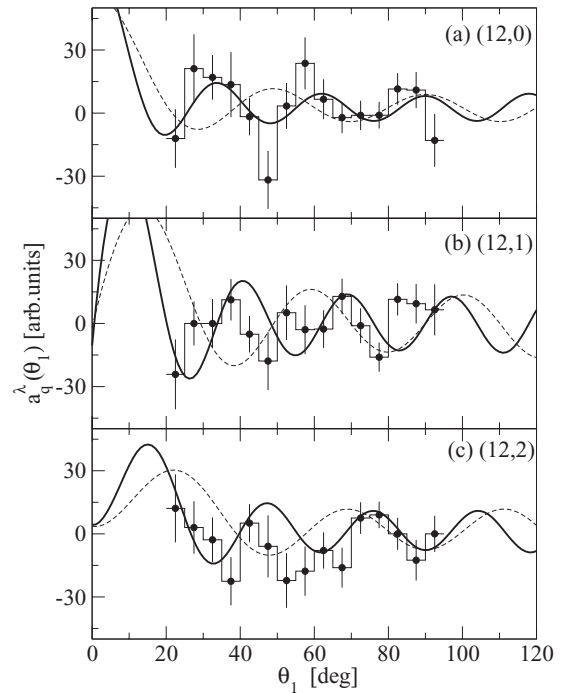
between two states at 18.97 MeV, assigned 8^+, and 19.21 MeV, assigned 9^-, which both decay toward the 2^+ level of ^{20}Ne. Despite the complexity of the spectrum, the angular correlation analysis of the 4^+ decay channel allowed for an unambiguous 10^+ assignment (see also Fig. 11).

The states observed in experiment B are listed in Table II (see also Fig. 4). It is worth noting that the spectra of states observed in experiments A and B show little overlap. This is attributable to the limits in kinematic acceptance of the respective setups. The spectrum obtained from experiment A, however, displays a good overlap with earlier experiments in the lower excitation regions [6,8,9]. The closest match to the conditions of experiment B is found in the work of Kelly *et al.* [19], where the α particles from the same reaction were observed at forward angles, but at a lower beam energy of 63 MeV. Kelly *et al.* focused on the angular distribution analysis of states decaying toward the ^{20}Ne ground state. We identify the 16.70- and 18.29-MeV 6^+ states of our experiment with the the 16.35- and 17.81-MeV, 6^+ levels of Kelly *et al.*, suggesting a discrepancy between the energy calibrations.

The detailed excitation function measurement of Becara *et al.* [20] lists the strongest states expected for the present beam energy as 16.60, 17.20, 19.22, 20.25, and 21.35 MeV, in close correspondence with the levels observed in experiment B (see also Fig. 4).

TABLE I. States in ^{24}Mg observed in experiment A, decaying by α particle emission. The spectrum of states includes results from Refs. [11,12,19–21] and the present work.

E_X (MeV)	E_{lit} (MeV)	Analyzed decay ^{20}Ne	I^π_{lit} ($\hbar$)	I^π ($\hbar$)
12.44	12.441 [21]	0^+	7^-	$6^+,7^-$
13.03	13.050 [21]	0^+	4^+	$(4,5)$
	13.055 [21]	0^+	5^-	(Doublet)
13.42	13.436 [21]	0^+	6^+	6^+
14.10	14.152 [21]	0^+	8^+	8^+
"	"	2^+		8^+
14.32	14.327 [21]	0^+	4^+	4^+
14.65	14.70 [20]	0^+		(4^+)
15.10	15.18 [20]	2^+	7^-	7^-
15.62	15.61 [20]	2^+		(6^+)
16.09	16.08 [8]	2^+	6^+	6^+
16.30[a]	16.29 [8,20]		8^+	
16.54	16.60 [20]	2^+	$8^+,9^-$	8^+
16.84[a]	16.84 [8]		8^+	
16.86	16.92 [20]	2^+		$(6^+,7^-)$
17.22	17.20 [20]	4^+		8^+
17.44	(17.63 [20])	2^+		$(6^+,7^-)$
17.90	17.87 [20]	2^+		8^+
18.16	18.11 [20]	2^+		8^+
18.97	[b]	2^+		8^+
19.07	19.22 [20]	4^+		10^+
19.21		2^+		9^-
20.09	20.25 [20]	4^+	(10^+) [4] (9^-) [22]	9^-
20.42	20.64 [20]	4^+		(9^-)

[a]State not observed in our experiment.

[b]State is not listed in [20], but peak visible in spectrum.

TABLE II. States in ^{24}Mg, observed in experiment B.

E_X (MeV)	E_{lit} (MeV)	Analyzed decay ^{20}Ne	I^π_{lit} ($\hbar$)	I^π ($\hbar$)
16.70(4)	16.35 [19]	0^+	6^+ [19]	6^+
	16.60 [20]			
17.29(4)	16.97 [19]	0^+		
18.29(4)	17.81 [19]	0^+	6^+ [19]	6^+
	18.11 [20]			
18.70(10)		0^+		
19.0(3)		2^+		
19.21(4)		0^+		
19.2(3)		2^+		
19.98(3)		0^+		7^-
19.92(8)		2^+		
20.25(3)	20.41 [19]	0^+	8^+7^- [19]	(8^+)
	20.25 [20]			
20.28(2)		2^+		
20.53(3)		0^+		6^+
20.46(1)		4^+		
20.68(5)		$2+$		
21.20(2)		2^+		
21.39(2)	21.39 [20]	0^+		6^+
21.46(2)		2^+		
21.66(5)		0^+		
21.80(1)		4^+		
22.79(2)		0^+		
22.87(1)		4^+		
23.00(2)		2^+		
23.10(3)		3^-		
23.26(1)		4^+		
23.77(1)		4^+		
24.53(5)		4^+		
24.60(3)		6^+		
24.98(14)		4^+		
25.40(3)		6^+		
26.28(2)		5^-		12^+
"		6^+		12^+
26.67(3)		6^+		(12^+)

The spectrum of experiment B reaches into a region of excitation energy where heavy ion resonances occur, as investigated, for instance, by Freer and coworkers [18]. In that work, ^{24}Mg high-spin resonances were populated in the ^{12}C(^{20}Ne,^{24}Mg*)^{8}Be reaction and detected through the ^{12}C + ^{12}C decay channel. Two 10^+ states were firmly established at 26.2(1) and 26.8(1) MeV, in close proximity to the 26.28(2)-MeV, 12^+, and 26.67(3)-MeV (12^+) levels in the present study. As our experiment also measured the ^{12}C + ^{12}C decay channel with significant efficiency, we were able to analyze the corresponding events, selected by similar methods as those described in Sec. II B. The corresponding excitation spectrum exhibited only small yields without clear resonance structures at the energies of interest. Nevertheless, the present data provided an upper limit upper limit of $\leqslant 5\%$ on the ^{12}C + ^{12}C decay branch relative to either of the α-decay channels. We conclude that we observe different states from those described in Ref. [18], presumably because of differences in the angular momentum barriers imparted in the reaction and the decay channels.

The combined data from experiments A and B establish a significantly enlarged spectrum of states in ^{24}Mg with firm spin and parity values, including the first experimentally identified 10^+_1 and 12^+ states.

VI. COMPARISON WITH SHELL-MODEL CALCULATIONS

Within the sd-shell orbital configurations allowed for ^{24}Mg, the maximum angular momentum that can be generated is 12. This value is reached by aligning the spins of all valence nucleons while obeying the constraints of the Pauli principle. This condition allows for only nine 12^+ states, of which six have isospin $T = 0$. Whether the experimental 12^+ states correspond to such aligned sd-shell configurations, or whether configurations involving the $f_{7/2}$ intruder shell are favored, is one of the questions arising from the present data.

Figure 15 displays the experimental energy spectrum of positive-parity states. The figure includes data for the 10^+_1, 12^+_1, and 8^+_4 levels established in this work. The spectrum is compared to the results of a shell model calculation limited to sd shell configurations, using the USDA interaction [26]. The USDA description of the experimental positive-parity spectrum is, in general, satisfactory, with a tendency to slightly
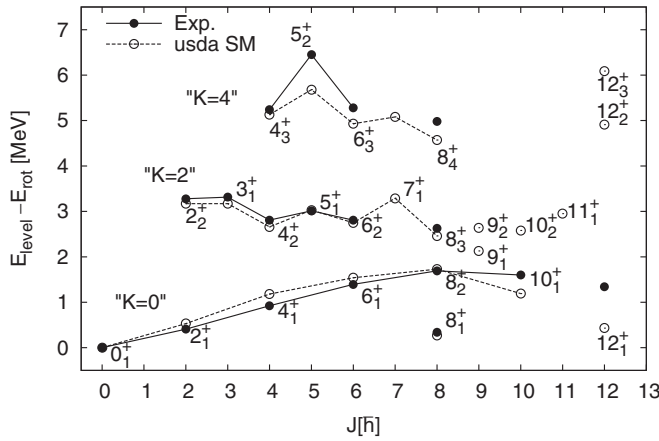
FIG. 15. Spectrum of experimental positive-parity states, from which a rotational energy $E_{\mathrm{rot}} = 0.16$ MeV $[I(I+1)]$ was subtracted to compress the energy scale. The experimental spectrum of states up to spin 6 was extracted from the ENSDF data base at the NNDC [23]. The states of spin 8 are taken from the Refs. [24] and [25] and the references listed in Table I. The 10^+ and 12^+ states are taken from Ref. [11] and the present work. The data are compared to a shell model calculation based on the USDA Hamiltonian.

underpredict the excitation energy of the highest-spin states, as manifested by the calculated energy of the 10^+ and 12^+ levels. A calculation with the USDB interaction [26] (not shown) predicts an almost identical spectrum for the states of Fig. 15. A striking feature present in both the USDA and USDB calculations is the large gap of more than 3.8 MeV between the lowest and the second lowest calculated 12^+ levels.

Figure 16 displays a map of ^{24}Mg states, categorized by their $d_{5/2}$ and $d_{3/2}$ occupation numbers as calculated with the
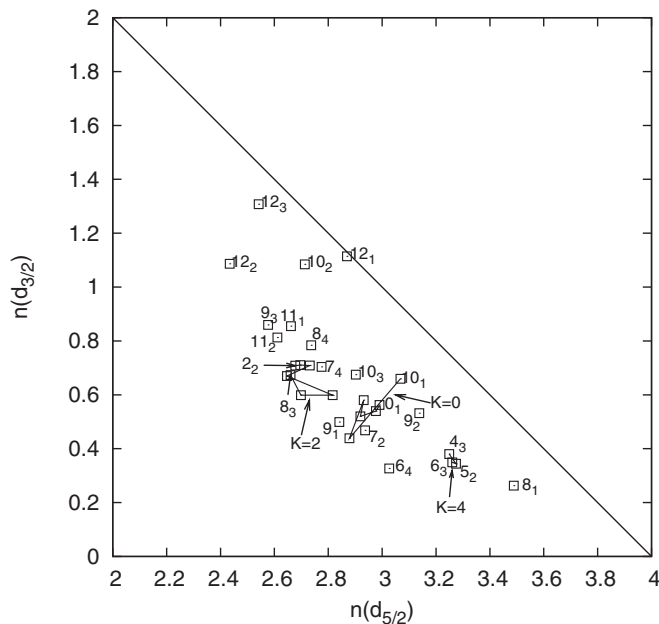

FIG. 16. Wave functions of ^{24}Mg states calculated using the USDA interaction, characterized by the occupation numbers of the $d_{5/2}$ and $d_{3/2}$ orbitals. All states lie below the diagonal because of the number of valence nucleons.
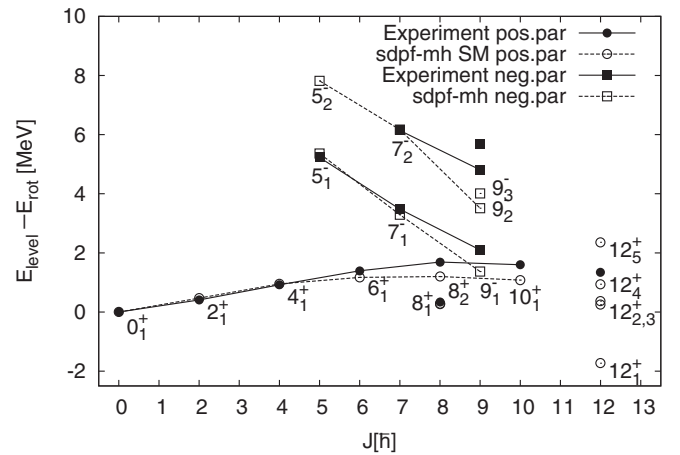

FIG. 17. Spectrum of the lowest experimental positive-parity and negative-parity states, compared with a calculation using the SDPF-MH Hamiltonian [27] (see text for details).

USDA Hamiltonian. A striking property is that band members, identified by their collective $B(E2)$ matrix elements, exhibit similar shell-model occupation numbers. The "$K = 2$" and "$K = 4$" bandheads were identified in the calculation through their lack of collective $B(E2)$ decay matrix elements. For states beyond spin 6, the K quantum numbers become strongly mixed. This is evident in the proximity of the $K = 0$ and $K = 2$ bands both energetically and in their wave-function configurations.

The calculations for the lowest 12^+ state indicate a wave function of essentially pure $d_{5/2}$ and $d_{3/2}$ character, very different from the "$K = 0$" rotational band, of which the 10_1^+ is a member. In the L-S coupling scheme, out of six $T = 0$, $J = 12^+$ levels, only one has the total spin $S = 0$. This configuration is a dominating component in the wave function of the 12_1^+ state in all sd shell-model Hamiltonians, contributing 54% in the USDA calculation. The $L = 12$, $S = 0$ configuration belongs to the (8,4) representation of the SU(3) symmetry group, where the state has a characteristic SU(3) label $K = 4$ [29,30]. The properties of the calculated configurations illustrate that the 12_1^+ is not a member of the $K = 0$ ground-state rotational band.

It is then natural to wonder to what extent 2p2h cross-shell excitations enter in the high-spin spectrum of positive-parity states. We performed shell-model calculations in a configuration space with the sd-shell, $0f_{7/2}$ and $1p_{3/2}$ orbitals. The results calculated with the SDPF-M interaction by Utsuno et al. [2], and the SDPF-MH interaction by Horoi [27] were compared. The SDPF-MH interaction, which was created following the procedure in described in Ref. [2], is available as an interaction file for the program COSMO [28]. For the purpose of our discussion, the SDPF-M and SDPF-MH interactions show only minor differences in excitation energy, that is, less than 150 keV.

In Fig. 17, the lowest positive- and negative-parity states are compared to a calculation with the SDPF-MH interaction. The spectrum of positive-parity states up to angular momentum 10 is very similar to the one obtained with the USDA interaction. This is also true of the states in the $K = 2$ and $K = 4$ structures

displayed in Fig. 15, which are omitted from Fig. 17 for clarity. An investigation of the corresponding wave functions reveals almost pure ($\geqslant 96\%$) sd-shell configurations. We also compared the negative-parity states above spin 5. These are expected to be dominated by configurations involving the $f_{7/2}$ orbital. The 5^-, 7^-, and 9^- states are predicted close to the experimental ones, with a tendency to overbind them at higher spin. We are including a 16.5-MeV level of angular momentum 9^-, which was not observed in our experiments, but was proposed in a $8^+, 9^-$ assignment to the 16.5-MeV doublet structure of Ref. [6].

In contrast to the USDA Hamiltonian, the 12_1^+ state is calculated to lie at 23.2 MeV, more than 3 MeV below the experimental level. Its dominant configuration contains one proton and one neutron each in the $f_{7/2}$ orbital. The 12_2^+ and 12_3^+ levels are nearly degenerate at 25.2 and 25.3 MeV of excitation. The 12_2^+ state shows an almost pure sd-shell wave function, whereas the 12_3^+ state has an $f_{7/2}$ intruder configuration. The SDPF-M interaction predicts the 12_2^+ and 12_3^+ states at nearly the same excitation energy, but in an inverted order with the 12_3^+ state being the sd-shell state. The near degeneracy of levels, confirmed by both shell-model calculations, indicates a very weak mixing, which is attributable to the extremely "stretched," exotic configuration of the 12^+ sd-shell state.

It should be noted that our experiment has little sensitivity to establish or exclude a 12^+ level as low as predicted by the SDPF-M or SDPF-MH interactions. Owing to barrier penetration properties, a 12^+ level at the calculated 23.2 MeV energy would likely decay toward the bound 4^+ state of ^{20}Ne. The corresponding experimental spectrum of ^{24}Mg states with this decay path (see Fig. 4) shows a number of prominent peaks in this energy region. These should be investigated in a future α-γ-γ angular correlation experiment.

VII. SUMMARY

High-spin states in ^{24}Mg have been measured with the ^{12}C(^{16}O, α)^{24}Mg reaction at beam energies of 62 and 68 MeV in two separate experiments. We developed an efficient method to analyze the angular correlations of multiparticle decay cascades by applying an orthogonal basis transformation, which has been presented here. We applied the data analysis method to our experiments, studying the high-spin spectrum of ^{24}Mg with the aim to establish levels approaching the terminating configuration of the sd shell with spin parity 12^+. The lowest known 10^+ and 12^+ states in ^{24}Mg were established as was a network of levels with unambiguously determined spin and parity. More detailed comparisons with theoretical models were enabled as a result.

The spectrum of positive-parity, high-spin states including the 10^+ and 12^+ states is in rather good agreement with the predictions of a shell-model calculation limited to sd-shell configurations using the USDA interaction. A more complex shell model calculation, extending the model space of the sd shell by the addition of the $0f_{7/2}$ and $1p_{3/2}$ orbitals and employing the SDPF-MH Hamiltonian, results in an almost equivalent description for the positive-parity states up to

angular momentum 10^+. While these states are exhibiting wave functions purely based on sd-shell configurations, the latter calculation also predicts a 12^+ state based on an $(f_{7/2})^2$ intruder configuration. However, the calculation places this state at an energy 3 MeV below the experimental and 2 MeV below the calculated nonintruder sd-shell 12^+ level. Our experiments were not sensitive to an intruder 12^+ state at such low excitation energy. A future experiment, optimized for this energy region and the decay paths expected for such a state, should be performed. The energetic position of cross-shell intruder states would provide additional information on the details of multishell descriptions of exotic nuclei.

APPENDIX : ANGULAR CORRELATION FUNCTION FOR α-α CASCADES

1. Density matrix approach

The description of the angular correlations between particles emitted in a process involving a common intermediate state is best addressed via the density matrix approach. In the latter, the particle emission from a given initial state I_1 to a state I_2; that is, $I_1 \rightarrow I_2$, leads to an ensemble of I_2 states $|\Psi\rangle$. This ensemble can be constrained by observables such as information on the initial state, the observation of a particle at a certain angle, or a certain polarization. Without any loss of generality, the ensemble of intermediate wave functions can be replaced by the corresponding density matrix. In the m-scheme basis $|\Psi\rangle = \sum_{m_2} \langle I_2 m_2 | \Psi \rangle | I_2 m_2 \rangle$, the density matrix is defined as

$$\rho_{m_2 m_2'}(I_2) = \frac{\sum_\Psi \langle I_2 m_2 | \Psi \rangle \langle \Psi | I_2 m_2' \rangle}{\sum_\Psi \langle \Psi | \Psi \rangle}.$$

The density matrix has an obvious set of properties: It is normalized, that is, $\text{Tr}\rho = 1$; it is also Hermitian $\rho = \rho^\dagger$, and an ensemble-average of any observable defined by an operator A is given by $\bar{A} = \text{Tr}(\rho A)$. Under basis transformation the density matrix transforms as any regular operator; that is, if $A' = U^{-1}AU$, then $\rho' = U^{-1}\rho U$.

In the following, we discuss the angular correlation function for the sequential emission of two α particles in a sequence of $I_1 \xrightarrow{\alpha_1} I_2 \xrightarrow{\alpha_2} I_3$, where the final state will, in practical applications, have spin and parity 0^+. To establish the angular correlation function, we first calculate the m-scheme density matrix of the intermediate state as a function of the α-particle emission angle.

2. Matrix element for the emission of an α particle

The first step in calculating the angular correlations of α particles is to identify the matrix element for its emission in a given spatial direction $\vec{k}$. The Coulomb and centrifugal barriers restrict the radial part of the α wave function to a nearly pure single angular momentum L. Thus, the common Coulomb phase shift is irrelevant. The matrix element of the transition operator $H_K(\theta, \phi)$ for emission of an α particle is

$$\langle I_2 m_2 | H_K(\theta_1, \phi_1) | I_1 m_1 \rangle$$
$$= \sqrt{4\pi} \sum_{Lm} \langle Lm | \Omega_1 \rangle \langle I_2 m_2 | H_m^L | I_1 m_1 \rangle, \quad (A1)$$

where the angular wave function in spherical-coordinate representation is given by the spherical harmonics, in accordance with the conventions of Ref. [15],

$$\langle \Omega | Lm \rangle = Y_m^L(\Omega).$$

The matrix element specified in Eq. (A1) allows us to calculate the density matrix of the state I_2 after the emission of the particle. The initial state is assumed to have an integer spin. In the following, we calculate the progression from the initial density matrix $\rho(I_1, m_{1a}, m_{1b}) = \delta(m_{1a}, 0)\delta(m_{1b}, 0)$ to the state I_2 through the emission of the α_1 particle detected at the angle $\Omega_1 = \{\theta_1, \phi_1\}$.

$$\rho_{m_2 m'_2}^{I_2}(\Omega_1) = N \langle I_2 m_2 | H_K(\Omega_1) | I_1 0 \rangle \langle I_1 0 | H_K(\Omega_1) | I_2 m'_2 \rangle,$$

The normalization coefficient is determined from the condition

$$\int d\Omega \sum_m \rho_{mm}^{I_2}(\Omega) = 1.$$

Using the Wigner-Eckart theorem we find the final expression for the density matrix as

$$\rho_{m_2 m'_2}^{I_2}(\Omega) = (2I_1 + 1) \sum_{m m'} (-1)^{m+m'} \begin{pmatrix} I_2 & L & I_1 \\ m_2 & m & m_1 \end{pmatrix}$$
$$\times \begin{pmatrix} I_2 & L & I_1 \\ m'_2 & m' & m_1 \end{pmatrix} \langle Lm | \Omega \rangle \langle \Omega | Lm' \rangle$$
$$= (-1)^{m_2 + m'_2} (2I_1 + 1) \begin{pmatrix} I_2 & L & I_1 \\ m_2 & -m_2 & 0 \end{pmatrix}$$
$$\times \begin{pmatrix} I_2 & L & I_1 \\ m'_2 & -m'_2 & 0 \end{pmatrix} \langle L - m_2 | \Omega \rangle \langle \Omega | L - m'_2 \rangle.$$
$$(A2)$$

Equation (A2) specifies the density matrix describing the intermediate state in the m scheme, where we have used $m_1 = 0$ as a maximally aligned initial state.

We now calculate the angular distribution of an α particle, labeled α_2, from the statistical ensemble of nuclei in the state I_2, which is specified by expression (A2) for the density matrix of the intermediate state I_2. Its emission leads to a new statistical density matrix $\rho_{m_3 m'_3}^{I_3}(\Omega_1, \Omega_2)$ of the final state I_3:

$$\rho_{m_3 m'_3}^{I_3}(\Omega_1, \Omega_2) = N \sum_{m2, m2'} \langle I_3 m_3 | H_K(\Omega_2) | I_2 m_2 \rangle \rho_{m_2 m'_2}^{I_2}(\Omega_1)$$
$$\times \langle I_2 m'_2 | H_K(\Omega_2) | I_3 m'_3 \rangle.$$

With a similar normalization,

$$\int d\Omega_1 d\Omega_2 \sum_m \rho_{mm}^{I_3}(\Omega_1 \Omega_2) = 1,$$

we obtain

$$\rho_{m_3 m'_3}^{I_3}(\Omega_1, \Omega_2) = (2I_2 + 1) \sum_{m_2 m'_2} \sum_{m m'} (-1)^{m+m'}$$
$$\times \begin{pmatrix} I_3 & L & I_2 \\ m_3 & m & m_2 \end{pmatrix} \begin{pmatrix} I_3 & L & I_2 \\ m'_3 & m' & m'_2 \end{pmatrix}$$
$$\times \langle Lm | \Omega_2 \rangle \langle \Omega_2 | Lm' \rangle \rho_{m_2 m'_2}^{I_2}(\Omega_1). \quad (A3)$$

In our analysis, we only consider final states of spin parity 0^+, which means that the final density matrix only has one element. Therefore, the angular correlation of the two α particles is given by this one element:

$$W(\Omega_1, \Omega_2) = \rho_{00}^{I_3}(\Omega_1, \Omega_2).$$

The previous expressions are given in a form that makes it possible to write the combined angular correlation function as

$$W(\Omega_1, \Omega_2) = \frac{2I_2 + 1}{2I_3 + 1} \sum_{m_2 m_{2'}} A_{m_2 m_{2'}}(I_1 \to I_2)(\Omega_1)$$
$$\times A_{m_2 m_{2'}}(I_3 \to I_2)(\Omega_2),$$

where

$$A_{m_2 m'_2}(I_1 \to I_2)(\Omega_1) = \rho_{m_2 m'_2}^{I_2}(\Omega_1).$$

Note that time reversal acts as

$$(2I_2 + 1) A_{m_2 m_{2'}}(I_3 \to I_2)(\Omega_2)$$
$$= (2I_3 + 1) A_{m_{2'} m_2}^*(I_2 \to I_3)(\Omega_2).$$

To arrive at the form most suited for our data analysis technique, we replace the complete summation in the m scheme by recoupling to the tensor indices λ and q, which lead to the so-called statistical tensor representation of the density matrix. This transformation is analogous to a recoupling of angular momentum vectors as $\vec{\lambda} = \vec{I'_2} - \vec{I_2}$. Introducing

$$A_q^\lambda(I_1 \to I_2)(\Omega_1) = (2\lambda + 1)^{1/2} \sum_{mm'} (-1)^{I_2 + m} \begin{pmatrix} I_2 & I_2 & \lambda \\ m & m' & q \end{pmatrix} A_{mm'}(I_1 \to I_2)(\Omega_1)$$

$$= (2\lambda + 1)^{1/2}(2I_1 + 1) \sum_{mm'} (-1)^{I_2 + m'} \begin{pmatrix} I_2 & I_2 & \lambda \\ m & m' & q \end{pmatrix} \begin{pmatrix} I_2 & L & I_1 \\ m & -m & 0 \end{pmatrix} \begin{pmatrix} I_2 & L & I_1 \\ m' & -m' & 0 \end{pmatrix} Y_{-m}^L(\Omega_1) \left(Y_{-m'}^L\right)^*(\Omega_1)$$

$$(A4)$$

and the time-reversed

$$B_q^\lambda(I_2 \to I_3)(\Omega) = (-1)^{\lambda-q} A_{-q}^\lambda(I_3 \to I_2)(\Omega),$$

the total angular correlation distributions probability becomes

$$W(\Omega_1, \Omega_2) = (2I_2 + 1) \sum_{\lambda q} A_q^\lambda(I_1 \to I_2)(\Omega_1) B_q^\lambda(I_2 \to I_3)(\Omega_2).$$

The explicit expression

$$B_q^\lambda(I_2 \to I_3) = \sum_{m,m'} (-1)^{I_2+m} (2\lambda+1)^{1/2} \begin{pmatrix} 0 & L & I_2 \\ 0 & -m & m \end{pmatrix} \begin{pmatrix} 0 & L & I_2 \\ 0 & -m' & m' \end{pmatrix} \begin{pmatrix} I_2 & I_2 & \lambda \\ -m & m' & q \end{pmatrix} Y_m^L(\Omega_2) (Y_{m'}^L)^*(\Omega_2) \quad (A5)$$

can be further simplified because the angular momentum of the final state is zero and thus $L = I_2$, so that product of first two $3j$ symbols reduces to $[(-1)^{m+m'}]/(2I_2 + 1)$. Recoupling of the product of spherical harmonics,

$$Y_m^L(\Omega)(Y_{m'}^L)^*(\Omega) = \sum_{\Lambda\mu} \frac{(2L+1)\sqrt{(2\lambda+1)}}{\sqrt{4\pi}} (-1)^{m'} \begin{pmatrix} L & L & \Lambda \\ 0 & 0 & 0 \end{pmatrix} \begin{pmatrix} L & L & \Lambda \\ m & -m' & \mu \end{pmatrix} [Y_\mu^\Lambda(\Omega)]^*, \quad (A6)$$

leads to

$$B_q^\lambda(I_2 \to I_3) = \sum_{m,m',\Lambda,\mu} (-1)^{I_2} \frac{2\lambda+1}{\sqrt{4\pi}} \begin{pmatrix} I_2 & I_2 & \lambda \\ -m & m' & q \end{pmatrix} \begin{pmatrix} I_2 & I_2 & \Lambda \\ -m & m' & -\mu \end{pmatrix} \begin{pmatrix} I_2 & I_2 & \Lambda \\ 0 & 0 & 0 \end{pmatrix} [Y_\mu^\Lambda(\Omega)]^*, \quad (A7)$$

where the complete sum over the m and m' indices reduces the product of the first two $3j$ symbols to $\delta(\lambda, \Lambda)\delta(q, -\mu)/\sqrt{2\lambda+1}$. We arrive at

$$B_q^\lambda(I_2 \to 0)(\Omega_2) = \frac{(-1)^{I_2+q}}{\sqrt{4\pi}} \begin{pmatrix} I_2 & I_2 & \lambda \\ 0 & 0 & 0 \end{pmatrix} Y_q^\lambda(\Omega_2). \quad (A8)$$

With its angular dependence reduced to a single spherical harmonic function, this description is suggestive of our data analysis technique, where the $B_q^\lambda(\Omega_2)$ tensor components are used as an orthogonal basis.

---

[1] F. Nowacki and A. Poves, Phys. Rev. C **79**, 014310 (2009).

[2] Y. Utsuno, T. Otsuka, T. Mizusaki, and M. Honma, Phys. Rev. C **60**, 054315 (1999).

[3] W. von Oertzen, M. Freer, and Y. Kanada-Enyo, Phys. Rep. **432**, 43 (2006), and references therein.

[4] A. H. Lumpkin, G. R. Morgan, J. D. Fox, and K. W. Kemper, Phys. Rev. Lett. **40**, 104 (1978).

[5] A. Szanto de Toledo, T. M. Cormier, M. M. Coimbra, N. Carlie Filho, P. M. Stwertka and N. G. Nicolis, Phys. Rev. C **30**, 1706 (1984).

[6] R. W. Zurmühle, D. P. Balamuth, L. K. Fifield, and J. W. Noé, Phys. Rev. Lett. **29**, 795 (1972).

[7] L. K. Fifield, R. W. Zurmühle, and D. P. Balamuth, Phys. Rev. C **8**, 2203 (1973).

[8] L. K. Fifield, R. W. Zurmühle, and D. P. Balamuth, Phys. Rev. C **8**, 2217 (1973).

[9] K. C. Young, R. W. Zurmühle, J. M. Lind, and D. P. Balamuth, Nucl. Phys. A **330**, 477 (1979).

[10] I. Wiedenhöver *et al.*, Phys. Rev. C **58**, 721 (1998).

[11] I. Wiedenhöver, A. H. Wuosmaa, R. V. F. Janssens, C. J. Lister, M. P. Carpenter, H. Amro, P. Bhattacharyya, B. A. Brown, J. Caggiano, M. Devlin, A. Heinz, F. G. Kondev, T. Lauritsen, D. G. Sarantites, S. Siem, and L. G. Sobotka, Nucl. Phys. A **682**, 22c (2001).

[12] I. Wiedenhöver, A. H. Wuosmaa, R. V. F. Janssens, C. J. Lister, M. P. Carpenter, H. Amro, P. Bhattacharyya, B. A. Brown, J. Caggiano, M. Devlin, A. Heinz, F. G. Kondev, T. Lauritsen, D. G. Sarantites, S. Siem, L. G. Sobotka, and A. Sonzogni, Phys. Rev. Lett. **87**, 142502 (2001).

[13] I. Y. Lee, Nucl. Phys. A **520**, 641c (1990).

[14] L. K. Fifield, D. M. Pringle, and W. J. Vermeer, Nucl. Phys. A **463**, 644 (1987).

[15] R. M. Steffen and K. Alder, in *The Electromagnetic Interaction in Nuclear Spectroscopy*, edited by W. D. Hamilton (North-Holland, Amsterdam, 1975).

[16] K. S. Krane, R. M. Steffen, and R. M. Wheeler, Nucl. Data Tables **11**, 5 (1973).

[17] S. P. G. Chappell, W. D. M. Rae, C. A. Bremner, G. K. Dillon, D. L. Watson, B. Greenhalgh, R. L. Cowin, M. Freer, and S. M. Singer, Phys. Lett. B **444**, 260 (1998).

[18] M. Freer, J. T. Murgatroyd, S. M. Singer, N. Curtis, D. J. Henderson, D. J. Hofman, and A. H. Wuosmaa, Phys. Rev. C **63**, 034317 (2001).

[19] G. R. Kelly, N. M. Clarke, M. Freer, B. R. Fulton, S. J. Hoad, R. A. Le Marechal, and R. E. Ward, Nucl. Phys. A **628**, 62 (1998).

[20] M. J. Bechara, A. J. Lazzarini, R. J. Ledoux, and E. R. Cosman, Phys. Rev. C **27**, 1540 (1983).

[21] R. Firestone and V. S. Shirley, *Table of Isotopes*, 8th ed. (Wiley & Sons, New York, 1996), Vol. I.

[22] M. J. LeVine, D. Branford, J. Barrette, and S. Kubono, J. Phys. G **10**, 1549 (1984).

[23] Data for ^{24}Mg extracted from the ENSDF database, revision of September 1, 2011, NNDC online service.

[24] D. Branford, M. J. Spooner, and I. R. Wright, Part. Nucl. **4**, 231 (1972).

[25] S. A. Wender, C. A. Gould, D. R. Tilley, D. G. Rickel, and R. W. Zurmühle, Phys. Rev. C **17**, 1365 (1978).

[26] B. A. Brown and W. A. Richter, Phys. Rev. C **74**, 034315 (2006).

[27] M. Horoi (private communication).

[28] A. Volya: Computer program COSMO [http://www.volya.net].

[29] M. Harvey, in *Advances in Nuclear Physics*, edited by M. Baranger and E. Vogt (Plenum Press, New York, 1968), Vol. 1.

[30] J. P. Draayer, Nucl. Phys. A **237**, 157 (1975).